

## Article

# A Multiphysics Simulation of the Effects of Wicking Geotextile on Mitigating Frost Heave under Cold Region Pavement

Yusheng Jiang <sup>1</sup>, Zaid Alajlan <sup>1</sup>, Claudia Zapata <sup>2</sup> and Xiong Yu <sup>1,\*</sup> 

<sup>1</sup> Department of Civil and Environmental Engineering, Case Western Reserve University, 2104 Adelbert Road, Bingham 203C, Cleveland, OH 44106, USA; zzs4@case.edu (Z.A.)

<sup>2</sup> School of Sustainable Engineering and the Built Environment, Ira A. Fulton Schools of Engineering, Arizona State University, Tempe, AZ 85042, USA; czapata@asu.edu

\* Correspondence: xxy21@case.edu

**Abstract:** Geotextile offers numerous benefits in improving pavement performance, including drainage, barrier functionality, filtration, and reinforcement. Wicking geotextile, a novel variant in this category, possesses the intrinsic ability to drain water autonomously from soils. This paper details the development and application of a comprehensive multiphysics model that simulates the performance of wicking geotextile within a pavement system under freezing climates. The model considers the inputs of various environmental dynamics, including the impact of meteorological factors, groundwater levels, ground heat, and drainage on the pavement system. The model was firstly validated using field data from a long-term pavement performance (LTPP) road section in the cold region. It was subsequently applied to assess the impacts of wicking geotextile if it was installed on the road section. The model simulated the coupled temporal and spatial variations in soil moisture content and temperature. The simulation results demonstrated that wicking geotextile would create a suction zone around its installation location to draw water from surrounding soils, therefore reducing the overall unfrozen water content in the pavement. The results also showed that the installation of wicking geotextile would delay the initiation of frost heave and reduce its magnitude in cold region pavement.



**Citation:** Jiang, Y.; Alajlan, Z.; Zapata, C.; Yu, X. A Multiphysics Simulation of the Effects of Wicking Geotextile on Mitigating Frost Heave under Cold Region Pavement. *Geosciences* **2024**, *14*, 34. <https://doi.org/10.3390/geosciences14020034>

Academic Editors: Meng Lu and Jesus Martinez-Frias

Received: 8 December 2023

Revised: 19 January 2024

Accepted: 23 January 2024

Published: 28 January 2024



**Copyright:** © 2024 by the authors. Licensee MDPI, Basel, Switzerland. This article is an open access article distributed under the terms and conditions of the Creative Commons Attribution (CC BY) license (<https://creativecommons.org/licenses/by/4.0/>).

**Keywords:** wicking geotextile; multiphysics modeling; frost heave mitigation; cold region; pavement

## 1. Introduction

The base and subgrade materials under pavement usually exhibit varied water content. The variation of moisture content may lead to adverse conditions such as shrinkage, heave, settlement, and fissure on pavement [1–3]. In addition, excessive water in pavement layers can result in a range of pavement distresses, including reduced strength and stiffness of geomaterials, soil particle erosion, freeze-thaw cycles, and durability cracking in concrete [4]. Wicking geotextile, a recent advancement in geosynthetic materials, offers a promising solution to these challenges in pavement structures [5]. Unlike traditional geotextiles, which primarily serve separation, filtration, and reinforcement purposes but offer limited efficacy in water drainage during unsaturated conditions, wicking geotextiles, composed of hydrophilic and hygroscopic nylon fiber yarns, exhibit the capability to laterally drain water in both saturated and unsaturated states [6–8]. The unique microstructure of wicking geotextile, marked by deep grooves with small openings, facilitates a higher capillary force and water transportation efficiency [8,9].

In practical engineering applications, geotextiles are typically installed within or at the base course bottom, extending to road slope surfaces [10]. The extended geotextile ends are exposed to the air to facilitate water evaporation, enhancing the driving force for drainage. In the cross-plane direction, the geotextile impedes upward movement of capillary water, protecting the overlying base course. In the in-plane direction, wicking geotextile absorbs

both free and capillary water from surrounding soils and laterally transports it to the extended end [11]. Laboratory tests have affirmed the superior drainage capabilities of wicking geotextiles in reducing soil water content [12–15]. Field tests have also validated the effectiveness of wicking geotextile in mitigating issues associated with water pumping [16], expansive soil [5], and frost heave [8].

The detrimental effects of soil freeze-thaw cycles on pavement, a complex multiphysics process of water transfer and phase transition, are pronounced in cold regions and contribute significantly to pavement damages [11,17–19]. Under freezing temperature, frost heave occurs in soil due to the growth of ice lens and volume expansion of water turning into ice [20], resulting in cracks and uneven surfaces. The subsequent thawing of ice causes local water enrichment, leading to localized soil strength reduction [21,22]. In addition, the ice lens melting can contribute to soil porosity increments with loose structure, therefore giving rise to pavement distresses by thaw settlement [23]. Effective drainage in cold regions is crucial to mitigate the adverse effects of freeze-thaw cycles on soil. Given the moisture control capabilities, wicking geotextile has shown great potential in enhancing pavement performance in these regions, as evidenced in field applications and site monitoring [24,25]. However, the intricacies of the coupled water variation process in pavement influenced by wicking geotextile remain relatively unexplored.

Numerical modeling serves as an effective tool for evaluating the interacted variations of moisture, heat, and stress-strain in unfrozen and frozen soils. While several models have been proposed to investigate these coupled processes, classifiable into thermal-hydro [26–30] models and thermal-hydro-mechanical [31–34] models, research integrating wicking geotextile within multiphysics models remains scarce [10]. This study introduces an advanced coupling model that assimilates various environmental dynamics, including meteorological, geothermal, and hydrological factors, and incorporates wicking geotextile to assess its impact on pavement under diverse environmental conditions. The highly non-linear partial differential equations of the model are solved using COMSOL5.5 (finite element solver). Initially, the model is validated with field data for a pavement case analysis without wicking geotextile. Subsequently, the wicking geotextile is incorporated into the same pavement case to simulate its effects on the frozen soil beneath the pavement.

## 2. Theoretical Background

The soil temperature and water content variation response to different environmental factors (e.g., ambient temperature, precipitation, solar radiation, etc.) are highly coupled processes in either frozen or unfrozen unsaturated soils. Following energy and mass conservation principles, two partial differential equations (PDE) govern the proposed model and form the theoretical basis of it, from where the water transport and thermal transfer in soil is described.

The transfer of heat in soil is evaluated by Fourier's equation:

$$C_a \frac{\partial T}{\partial t} = \nabla(\lambda \nabla T) \quad (1)$$

where  $C_a$  represents the apparent volumetric heat capacity in  $J/(m^3 \cdot K)$ ,  $T$  represents the temperature in  $K$ ,  $t$  represents time, and  $\lambda$  represents thermal conductivity in  $W/(m \cdot K)$ . In Equation (1),  $C_a$  and  $\lambda$  are phases-ratio dependent. To reduce computation nonlinearity, the apparent heat capacity  $C_a$  [35] is taken in the model to consider the energy absorption and release during phase transition by:

$$C_a = C_s \theta_s + C_w \theta_w + C_i \theta_i + C_v (n - \theta_w - \theta_i) - L_f \rho_i \frac{d\theta_i}{dT} \quad (2)$$

where subscripts  $i$ ,  $s$ ,  $w$ , and  $v$  denote ice, soil solid, unfrozen water, and air phase separately;  $\theta$  is volumetric content of different phases;  $C$  is heat capacity of different phases in  $J/(m^3 \cdot K)$ ;  $L_f$  is latent heat in  $J/kg$ ; and  $\rho_i$  represents density of ice in  $kg/m^3$ .  $\lambda$  is evaluated by

Equation (3) considering the impact of solid soil, liquid moisture, ice, and air on heat transport [28,36,37]:

$$\lambda = \lambda_s^{\theta_s} \lambda_w^{\theta_w} \lambda_i^{\theta_i} \lambda_a^{\theta_a} \quad (3)$$

where the subscripts have same meanings as those of heat capacity in Equation (2).

The mass migration in the partially saturated porous media is evaluated by a modified Richards' equation:

$$\frac{\partial \theta_w}{\partial t} + \frac{\rho_i}{\rho_w} \frac{\partial \theta_i}{\partial t} = \nabla (K_{Lh} \nabla h + K_{Lh} i + K_{LT} \nabla T) \quad (4)$$

where  $\rho_w$  denotes the water density in  $\text{kg}/\text{m}^3$ ,  $K_{Lh}$  and  $K_{LT}$  are the hydraulic conductivity related to pore pressure and temperature gradient in  $\text{m}/\text{s}$ ,  $h$  denotes the matric suction in  $\text{m}$  (water pressure unit), and  $i$  denotes the unit vector along gravity direction.

The soil-water characteristics curve (SWCC) by Van Genuchten [38] is utilized to describe the relationship between unfrozen water content and suction for either unfrozen or frozen soil [39,40]. The hydraulic conductivity in Equation (4) is calculated through Van Genuchten's equations as suggested by [28]:

$$S_e = \frac{\theta - \theta_r}{\theta_s - \theta_r} = (1 + |\alpha h|^n)^{-m} \quad (5)$$

$$K_{Lh} = K_s S_e^l \left[ 1 - \left( 1 - S_e^{\frac{1}{m}} \right)^m \right] \quad (6)$$

$$K_{LT} = K_{Lh} \left( \frac{h G_{wT} d\gamma}{\gamma_0 dT} \right) \quad (7)$$

$$K_{fLh} = 10^{-\Omega Q} K_{Lh} \quad (8)$$

where  $S_e$  represents the effective saturation,  $\theta_r$  and  $\theta_s$  denote the residual and saturated water content in percentage,  $\alpha$ ,  $m$ ,  $n$ , and  $l$  are material-specified constants specific to the material as determined by the SWCC,  $K_s$  is the saturated hydraulic conductivity measured in  $\text{m}/\text{s}$ ,  $\gamma$  signifies the surface tension of soil water in  $\text{gs}^2$  varying with temperature and calculated as  $\gamma = 75.6 - 0.145T - 2.38 \times 10^{-4}T^2$  ( $T$  is in  $\text{degC}$ ),  $K_{fLh}$  refers to the hydraulic conductivity linked to the pore pressure head in frozen soil in  $\text{m}/\text{s}$  accounting for the obstructive effect of ice on moisture movement,  $\Omega$  is an impedance factor contingent on the type of material, and  $Q$  represents the ratio of  $\theta_i$  to  $\theta_i + \theta_s - \theta_r$ . Equation (4) determines the volumetric ice content using empirical formulas [41,42]:

$$B(T) = \frac{\theta_i}{\theta_w} = \begin{cases} \frac{\rho_w}{\rho_i} \left( \left| \frac{T}{T_f} \right|^b - 1 \right) & (T < T_f) \\ 0 & (T \geq T_f) \end{cases} \quad (9)$$

$$\theta_i = B(T) * \theta_w \quad (10)$$

where  $B$  represents the ratio of volumetric ice content to unfrozen water content,  $T$  denotes the temperature measured in  $K$ ,  $T_f$  stands for the freezing point in  $K$ , and  $b$  signifies empirical coefficients related to the soil type with specified values of 0.56 for clay, 0.47 for silt, and 0.61 for sand and gravel.

The proposed model integrates various environmental effects. For the thermal aspect, it considers effects including solar short-wave radiation, upward longwave radiation, air temperature, wind speed, relative humidity, and ground heat flux, which are factored in using Neumann boundary conditions. In the hydraulic domain, the model incorporates the effects of precipitation, evaporation on geotextile, and changes in groundwater elevation,

which are addressed through either Neumann or Dirichlet boundary conditions. The absorption of shortwave solar radiation on the structure surface can be described by [43]:

$$q_s = (1 - albedo) * S \quad (11)$$

where  $q_s$  denotes the short-wave absorption of the solar radiation, the albedo refers to the solar reflectivity, and  $S$  represents the solar radiation in  $W/m^2$ . The total long-wave radiation, which encompasses both outgoing radiation and counter-radiation, is evaluated by the Stefan–Boltzmann law [44]:

$$q_l = \epsilon\sigma T_s^4 - \epsilon_a\sigma T_{sky}^4 \quad (12)$$

$$T_{sky} = \left(0.754 + 0.0044T_{dp}\right)^{0.25} * T_{amb} \quad (13)$$

$$T_{dp} = T_{amb} - \frac{100 - RH}{5} \quad (14)$$

where total  $q_l$  represents the long-wave radiation,  $\epsilon$  signifies the emission coefficient, and  $\epsilon_a$  denotes the absorption coefficient of pavement. For simplicity in analysis, it is assumed that  $\epsilon = \epsilon_a$ . The Stefan-Boltzmann constant,  $\sigma$ , is equal to  $5.68 * 10^{-8} W * m^{-2} * K^{-4}$ ,  $T_s$  is the pavement surface temperature measured in  $K$ ,  $T_{sky}$  is the effective ambient temperature above the structure in  $K$ ,  $T_{dp}$  represents the dewpoint temperature in  $K$  at which air becomes saturated when cooled, and  $RH$  is relative humidity in percentage.  $T_{amb}$  is the ambient air temperature in  $K$ . Additionally, as mentioned in Equation (13), the effect of the ambient air temperature, along with wind speed, is also revealed in the convective heat flux on structure surface via Newton's law of cooling [45]:

$$n \cdot (\lambda \nabla T) = h_c (T_{amb} - T) \quad (15)$$

$$\begin{cases} h_c = 5.6 + 4 * v_{wind} & \text{for } v_{wind} \leq 5 \text{ m/s} \\ h_c = 7.2 + 4 * v_{wind}^{0.78} & \text{for } v_{wind} > 5 \text{ m/s} \end{cases} \quad (16)$$

where  $n$  represents the normal unit vector perpendicular to the boundary surface,  $\lambda_c$  denotes the thermal conductivity in  $W/(m \cdot K)$ ,  $T$  indicates the temperature at boundaries in  $K$ , and  $h_c$  is the convection heat transfer coefficient in  $W/(m^2 \cdot K)$ . The ground heat flux is calculated by:

$$q_g = n \cdot \lambda_{bottom} \nabla T_{bottom} \quad (17)$$

where  $\lambda_{bottom}$  and  $\nabla T_{bottom}$  are the thermal conductivity in  $W/(m \cdot K)$  and temperature gradient in  $K/m$  of the material right at bottom boundary, respectively.

In the hydraulic field, Horton's empirical equation [46] is used to evaluate the infiltration capacity as well as infiltration rate via Neumann boundary condition. The GWT is usually located at the interface where the positive and negative pore water pressure is separated with zero water pressure on. Hence, Dirichlet boundary condition is added on the bottom boundary to represent the effect of the equivalent GWT change. The drainage effects of wicking geotextile can be simulated via assigning either Neumann boundary [10] or Dirichlet boundary [7], depending on the geometry assumptions and solving stability. In current studies, a Dirichlet boundary condition is utilized to simulate the evaporation effect on the extended geotextile end.

### 3. Model Validation

To validate the model, a case analysis is performed for the LTPP section 46-0804. The site measured subgrade gradation, water content, and temperature data, all of which indicated that the soil below the section is frost susceptible. In addition, the SMP database has well-documented site-measured time series data of climate, temperature, and moisture content of this section, hence its selection for the case analysis. The case study first verifies the proposed model for the pavement without geotextile, then it simulates the installation

of geotextile in the same pavement system to study the effect of the wicking geotextile. The filed data are collected from SMP database. The geometry of the pavement is shown in Figure 1, which includes a three-layer structure in a two-dimensional form. The detailed layer information is summarized in Table 1.

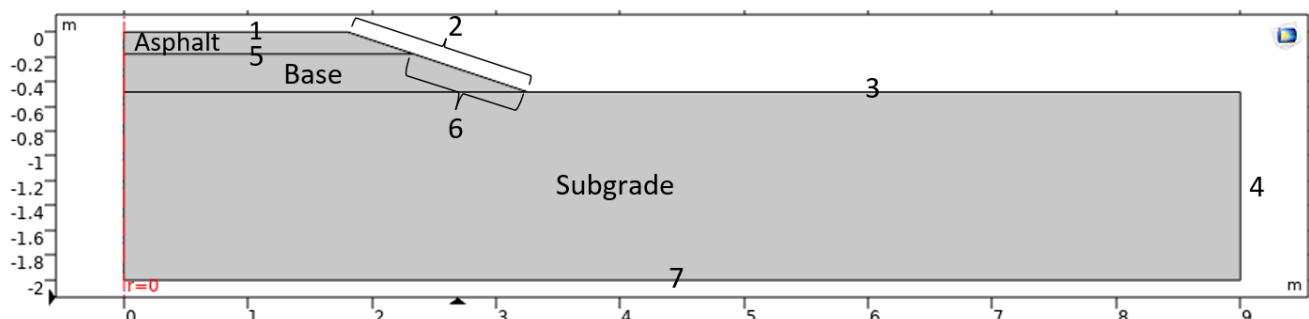


**Figure 1.** Geometry of the three-layer pavement system without geotextile.

**Table 1.** Layer information.

| Layer # | Material   | Thickness (m) |
|---------|--|---------------|
| 3       | Asphalt concrete: hot mixed, hot laid AC, dense graded | 0.180         |
| 2       | Unbound (granular) base: crushed stone                 | 0.305         |
| 1       | Subgrade (untreated): fine-grained soils: silty clay   | 1.515         |

The analysis includes boundary conditions for various environmental factors, assessing the impacts of air temperature, solar short-wave radiation, precipitation, wind velocity, relative humidity, geothermal temperature gradient, and groundwater table elevation. To model the energy transfer between the atmosphere and the pavement surface, the upper three boundaries (boundaries one to three, as shown in Figure 1) are subjected to fluxes from short-wave radiation, long-wave radiation, and air convection. The temperature gradient at the lower boundary is calculated using temperature measurements taken near a depth of two meters, as shown in Figure 2c. This measurement facilitates the calculation of time-varying geothermal flux. The geothermal influence is incorporated by applying a Neumann boundary condition at boundary seven using this flux. Considering the low rainfall intensity and relative high soil permeability, the infiltration capacity is presumed to always exceed rainfall intensity, implying that water flux due to precipitation is the same as the rainfall intensity in the analyzed case. This precipitation flux is applied to boundaries three, five, and six. The GWT effects are simulated by assigning pressure head (Dirichlet boundary) to boundary seven. The right boundary (boundary four in Figure 1) is assumed to be both thermally and hydraulically insulated.

For the model verification case, a 220-day analysis was conducted starting from 1 September 2000 and ending 15 March 2001. The temporal variation of air temperature, precipitation, solar short-wave radiation, wind speed, and relative humidity are shown in Figure 2.

Table 2 presents the simulation's needed parameters, including the parameters of geotextile, pavement surface material, and soil layers. These parameters are found or calculated using site measured data from the LTPP database and literature [7,34,47]. The SWCC and hydraulic conductivity variation with suction of base, subgrade, and wicking geotextile are presented in Figure 3 with data from [7].

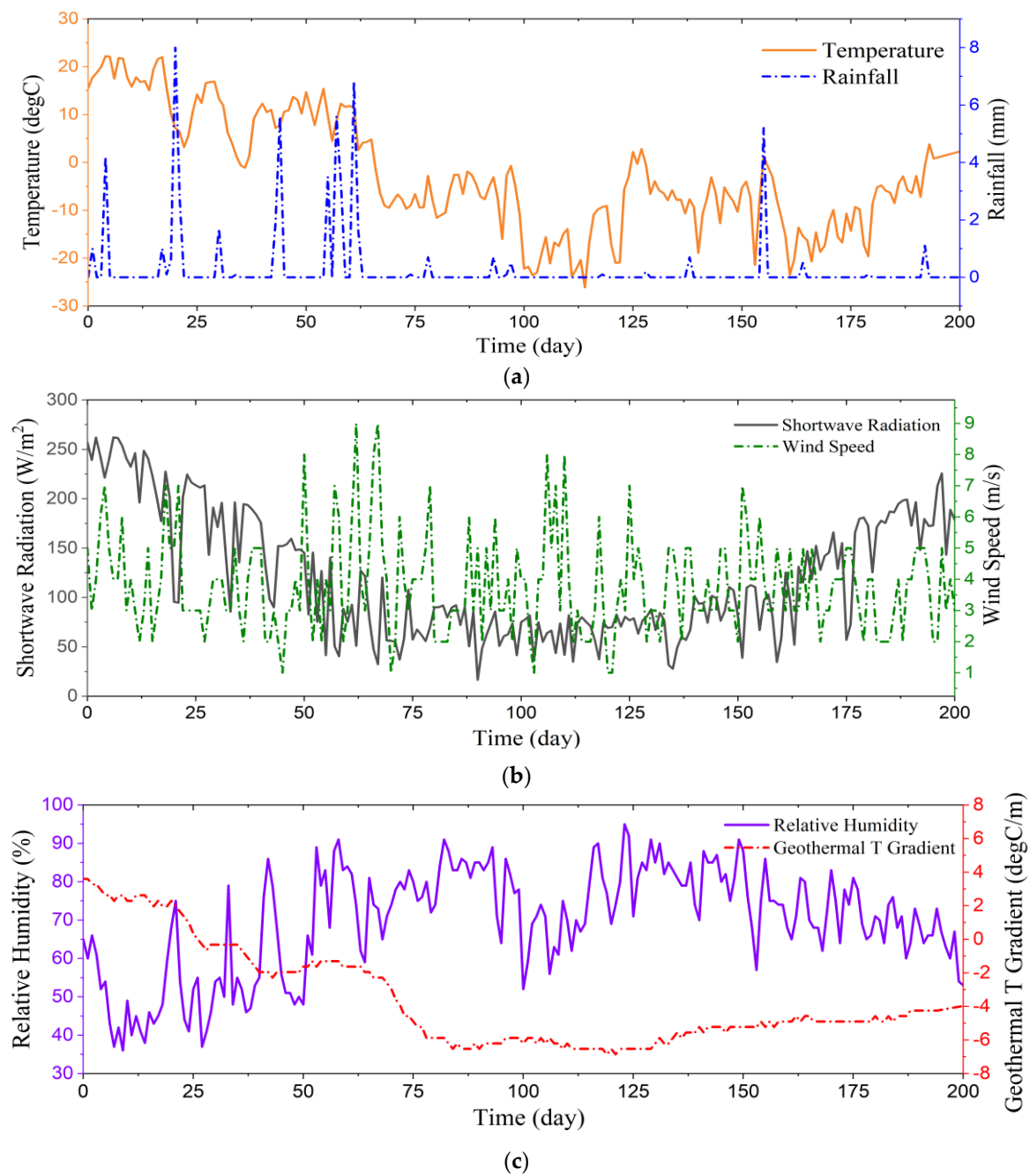


**Figure 2.** Temporal changes in climatic and environmental factors from 1 September 2000 to 15 March 2001: (a) air temperature and precipitation, (b) solar short-wave radiation and wind velocity, and (c) relative humidity and temperature gradient related to geothermal heat.

**Table 2.** Constant parameters of calculation example.

| Symbol      | Value (Unit)                              | Description                                 |
|-------------|---|---|
| $C_i$       | $1.9 \times 10^6$ [J/(m <sup>3</sup> *K)] | Volumetric heat capacity of ice             |
| $C_n$       | $2.0 \times 10^6$ [J/(m <sup>3</sup> *K)] | Volumetric heat capacity of solid           |
| $C_v$       | $1.2 \times 10^3$ [J/(m <sup>3</sup> *K)] | Volumetric heat capacity of air             |
| $C_w$       | $4.2 \times 10^6$ [J/(m <sup>3</sup> *K)] | Volumetric heat capacity of liquid          |
| $C_{pp}$    | $2.3 \times 10^6$ [J/(m <sup>3</sup> *K)] | Heat capacity of pavement surface layer     |
| $\lambda_p$ | 1.1 [W/(m*K)]                             | Heat conductivity of pavement surface layer |
| $L_f$       | $3.3 \times 10^5$ [J/kg]                  | Freezing latent heat                        |

Table 2. Cont.

| Symbol        | Value (Unit)                          | Description   |
|---------------|---------------------------------------|---|
| $L_0$         | $3.3 \times 10^8$ [J/m <sup>3</sup> ] | Volumetric freezing latent heat                     |
| $\gamma_0$    | 71.9 [g/s <sup>2</sup> ]              | Surface tension of soil water at 25° Celsius        |
| $\rho_i$      | 931 [kg/m <sup>3</sup> ]              | Density of ice                                      |
| $\rho_n$      | 2700 [kg/m <sup>3</sup> ]             | Density of soil mass                                |
| $\rho_w$      | 1000 [kg/m <sup>3</sup> ]             | Density of water                                    |
| $g$           | 9.8 [m/s <sup>2</sup> ]               | Acceleration due to gravity                         |
| $K_{s1}$      | $1.3 \times 10^{-3}$ [m/s]            | Saturated hydraulic conductivity of base            |
| $K_{s2}$      | $1.1 \times 10^{-7}$ [m/s]            | Saturated hydraulic conductivity of subgrade        |
| $K_{sw}$      | 0.001 [m/s]                           | Saturated hydraulic conductivity of geotextile      |
| $\theta_{s1}$ | 0.36                                  | Saturated volumetric moisture content of base       |
| $\theta_{s2}$ | 0.50                                  | Saturated volumetric moisture content of subgrade   |
| $\theta_{sw}$ | 0.33                                  | Saturated volumetric moisture content of geotextile |
| $\theta_{r1}$ | 0.075                                 | Residual volumetric moisture content of base        |
| $\theta_{r2}$ | 0.01                                  | Residual volumetric moisture content of subgrade    |
| $\theta_{rw}$ | 0.04                                  | Residual volumetric moisture content of geotextile  |
| $\epsilon_a$  | 0.95                                  | Absorption coefficient on pavement surface          |
| $\epsilon$    | 0.95                                  | Emission coefficient on pavement surface            |
| albedo        | 0.22                                  | Solar reflectivity                                  |

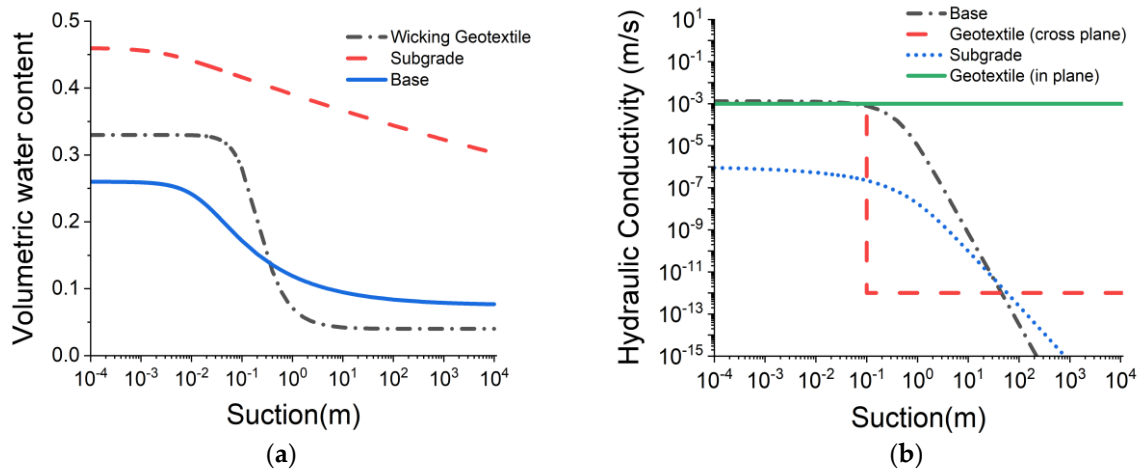
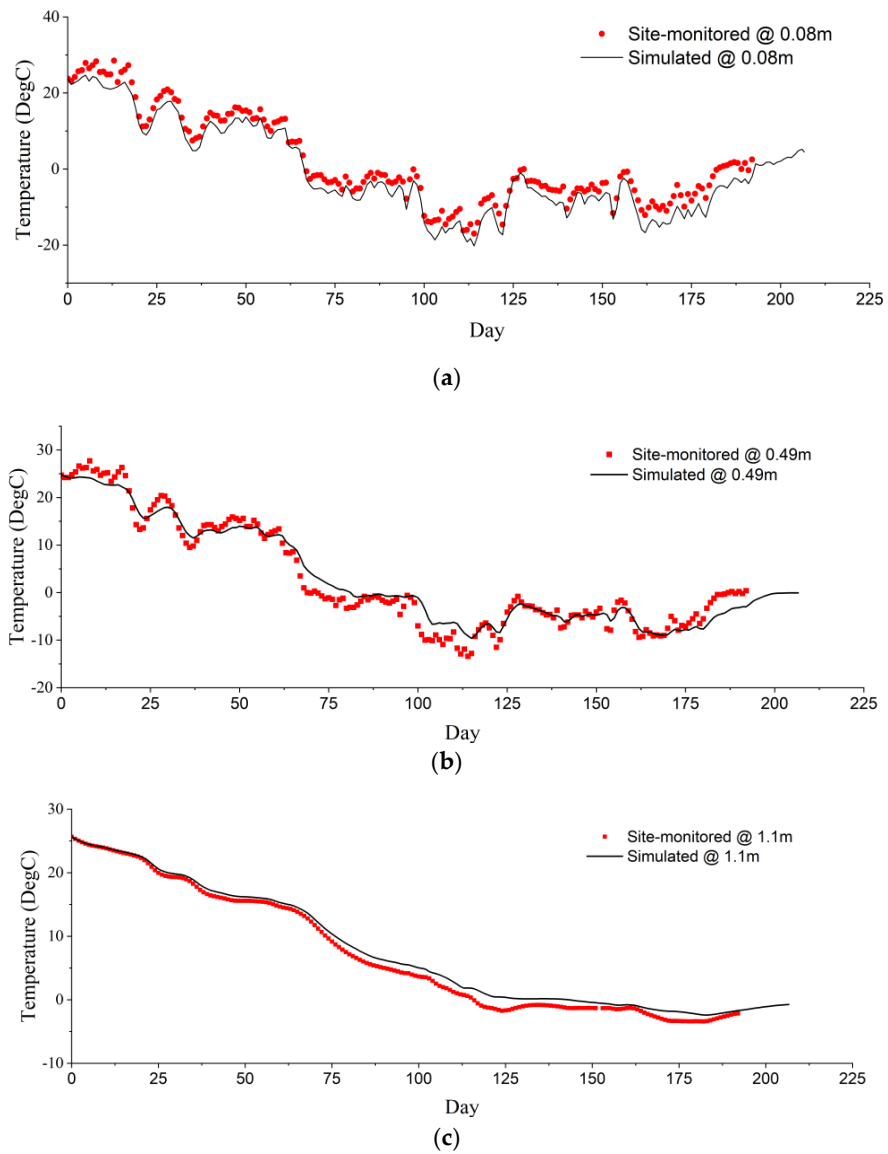
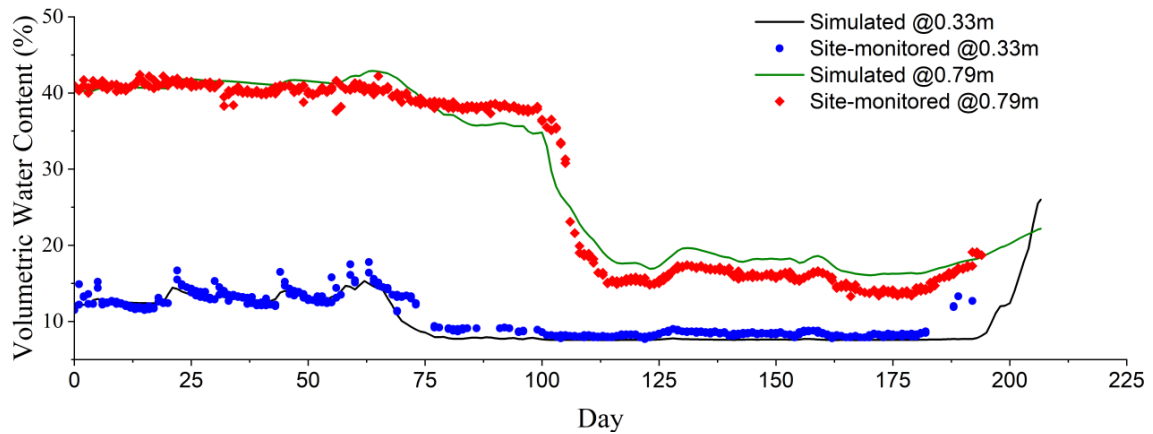


Figure 3. (a) SWCC of base, subgrade, and wicking geotextile, (b) hydraulic conductivity vs. suction of base, subgrade, and wicking geotextile.

The temperature, water content, and frost depth variation with depth and time are calculated by the proposed model. The results are compared with site-monitored data as shown in Figures 4–6, which shows closely matched values. This validates the model’s performance to simulate the thermal and hydraulic field response of soil to environmental dynamics for the analyzed case. More detailed information about model validations can be found in [19].



**Figure 4.** Comparison of simulated and actual temperatures over time: (a) at a depth of 0.08 m in asphalt layer, (b) at a depth of 0.49 m in base layer, and (c) at a depth of 1.1 m in subgrade layer (along the axis of symmetry of the pavement).



**Figure 5.** Comparison of simulated and actual temperatures over time at depth of 0.33 m in base layer and 0.79 m in subgrade layer (along the axis of symmetry of the pavement).

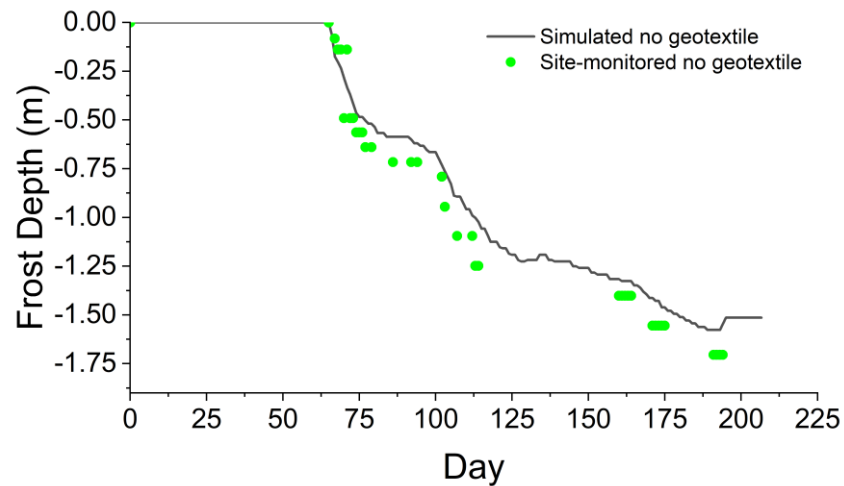


Figure 6. Simulated and site-measured frost depth (below pavement slope top) vs. time.

#### 4. The Effects of Wicking Geotextile on Frost Heave Mitigation

Based on the verified case, a model with wicking geotextile is then simulated. Identified boundary conditions, layer parameters, and model settings are simulated as the validation case study is utilized. In this model, the geotextile is simplified as a domain layer that is three centimeters thick, as shown in Figure 7. A 6.6 m length geotextile is assumed to be buried at a depth  $-1.5$  m from the pavement surface and on the interface between the base and the subgrade layer. Referring to [7], to simulate the drainage effect of the evaporation on the wicking geotextile end, a constant pressure head of 200 kPa boundary is added on the right end of the geotextile layer (a Dirichlet line boundary). Figure 8 shows the simulated suction and water flow direction comparison between pavement with and without geotextile, where results of time at the start of simulation (first day) and after a rainfall event (twenty-fifth day) are presented. The black arrows in Figure 8 point out the direction of water flow. As shown in Figure 8, the wicking geotextile can influence the suction distribution apparently. Figure 8b,d show obvious higher suction in zones along the geotextile, reflecting the pumping effects. The arrow direction indicates the water in surrounding soils are absorbed and flow toward the wicking geotextile. The zoomed-in figure displays the simulated unfrozen water migration direction inside of the geotextile, where the unfrozen water transport horizontally and drained out to the right side.

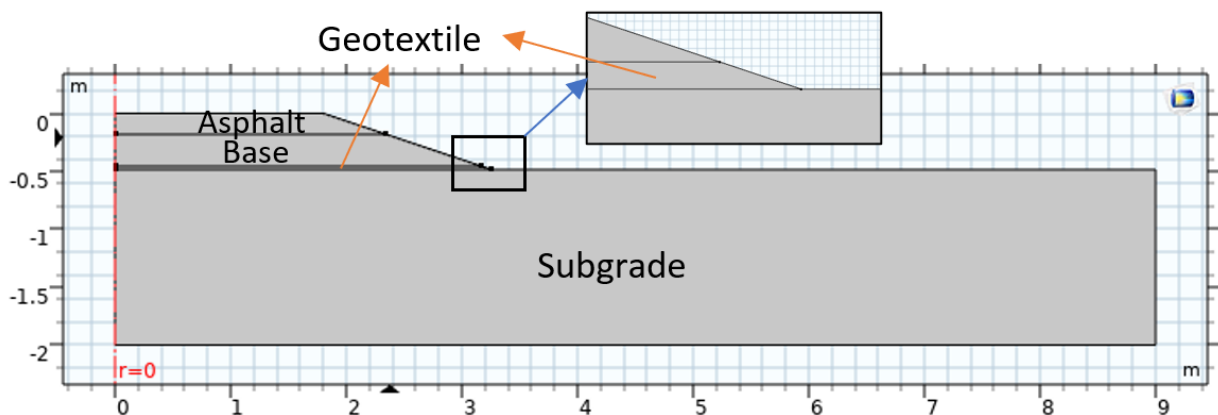
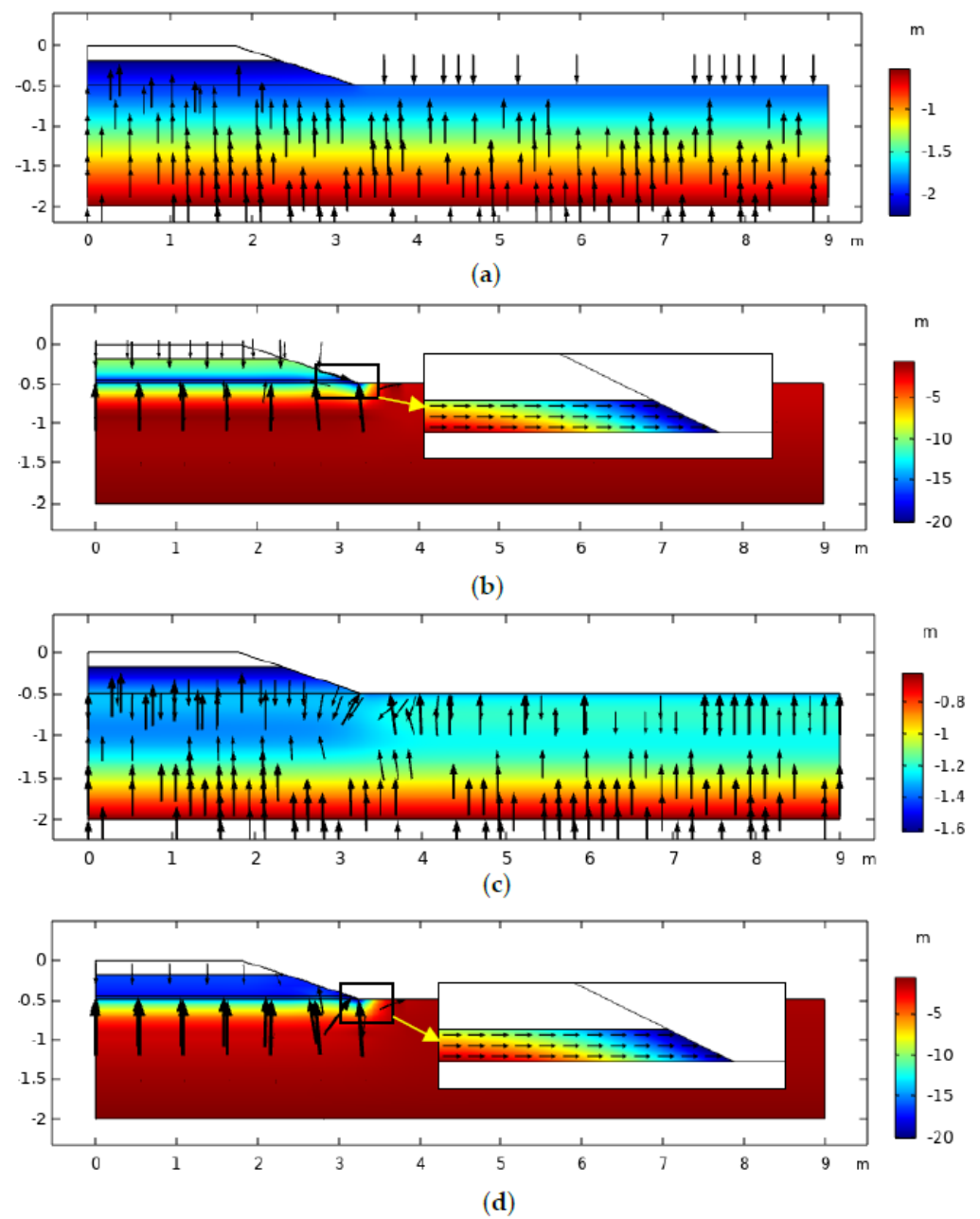


Figure 7. Geometry of the three-layer pavement system with geotextile.



**Figure 8.** Simulated suction (pressure in m water) distribution and water flow direction on: (a) first day without geotextile, (b) first day with geotextile, (c) twentieth day without geotextile, and (d) twentieth day with geotextile.

Figure 9 shows the moisture content variation comparison between the pavement with and without geotextile. According to results of Figure 9, the wicking geotextile effectively decreases water content from the start of the simulation at both 0.33 m depth and 0.79 m depth. The obvious drop of water content around the 70th day at 0.33 m and the 100th day at 0.79 m are induced by water freezing. Note that Figures 5 and 9 merely present unfrozen water content and the TDR sensor only recorded unfrozen water content in the LTPP database. The expanded volumetric content is defined as the total volumetric water content (summation of volumetric unfrozen water content and ice content) during freezing minus the porosity of the soil. Assuming the frost heave occurred when the total volumetric water content exceeds the porosity, frost heave can be evaluated by integration of the expanded volumetric content along vertical direction. Based on the model-simulated volumetric unfrozen and frozen water content, the frost heave along the pavement center

line is estimated and compared in Figure 10. As indicated in Figure 10, the geotextile delays the time of frost heave initiation and mitigates the magnitude of frost heave with time.

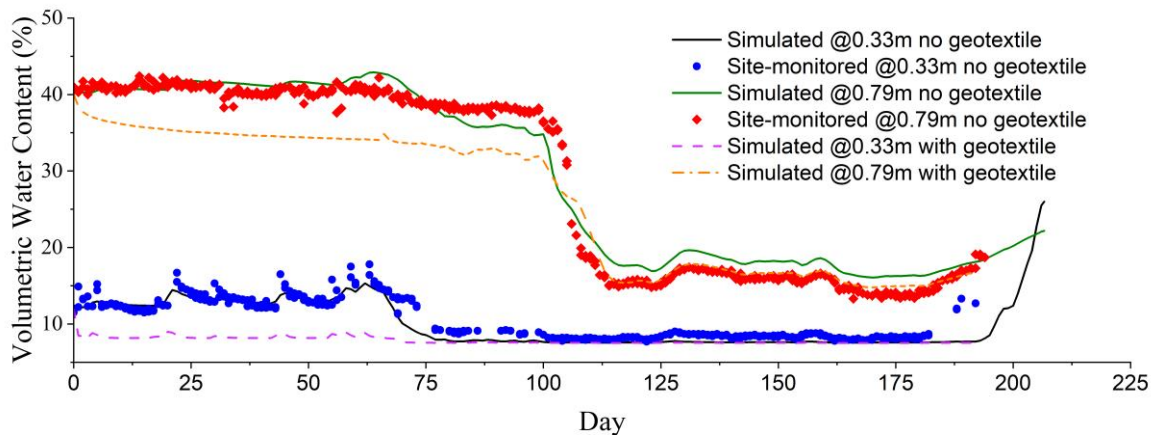


Figure 9. Water content vs. time at 0.33 m and 0.97 m depth, with and without geotextile.

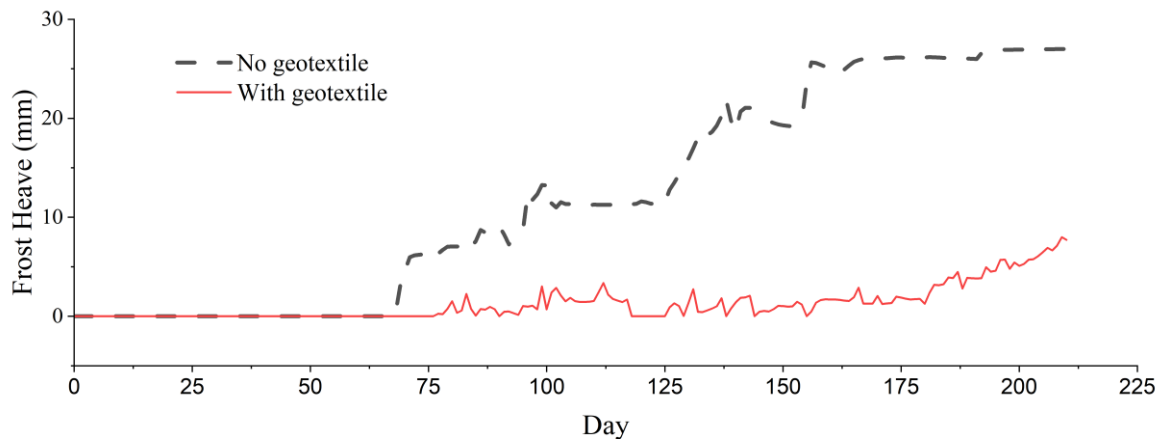
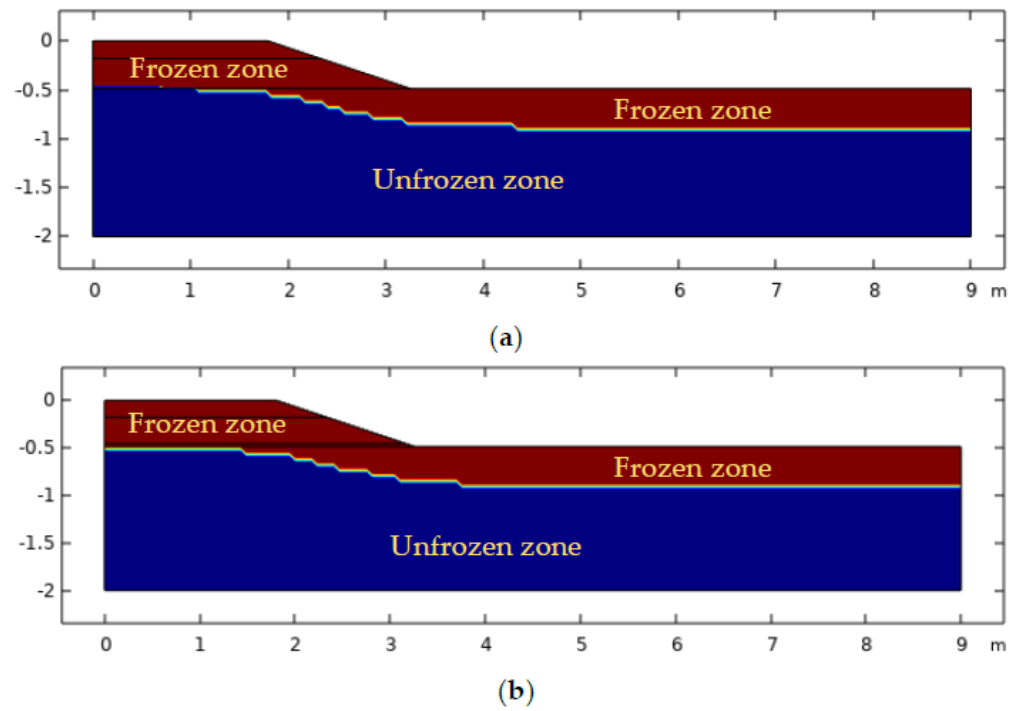
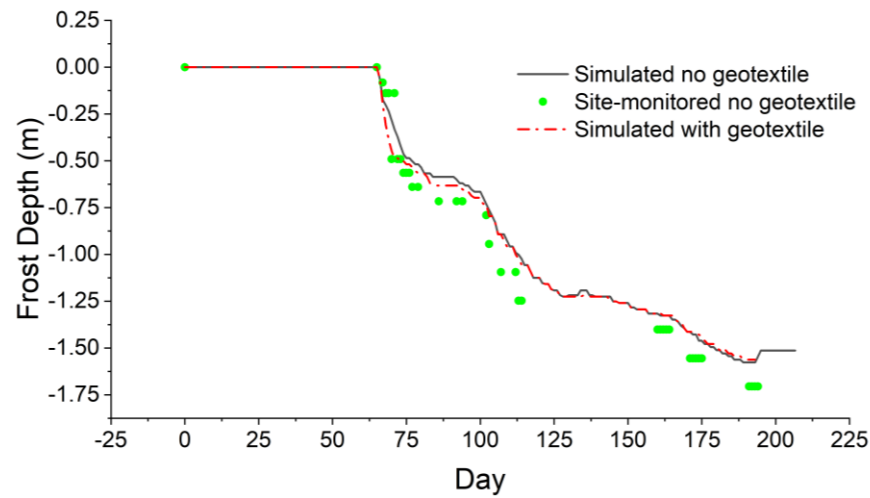


Figure 10. Frost heave (along pavement axis of symmetry) without geotextile installation and with geotextile installation.

According to the simulated results, it is interesting to note that geotextile has inappreciable effect on frost depth. Figure 11 shows the freezing conditions on the 80th day. It classifies the pavement into a frozen zone (with red color) and an unfrozen zone (with blue color) based on the freezing temperature of pore soil water. As seen in Figure 11, the wicking geotextile has barely any impact on frost depth distribution in pavement and ground. Although the wicking geotextile removes the soil water from the subgrade (Figure 9) and decreases the heat capacity, the induced larger volumetric air content decreases the soil thermal conductivity at the same time. As a result, the ground freezing speed does not change greatly, and frost depth is not significantly influenced. This conclusion can also be supported by Figure 12, which displays the frost depth vs. time, with and without geotextile.



**Figure 11.** Frost depth spatial distribution comparison between (a) without geotextile installation and (b) with geotextile installation on the 80th day in simulation.



**Figure 12.** Frost depth (below pavement slope top) vs. time, with and without geotextile.

The simulated temperature variations over time, both with and without the geotextile, are compared at various depths of each pavement layer. As depicted in Figure 13, the simulations reveal that the wicking geotextile exerts a negligible influence on temperature fluctuations over time. This observation aligns with the findings presented in Figures 11 and 12. A marginal decrease in temperature was noted between the 62nd and the 112nd days in the presence of the geotextile. This slight temperature reduction is likely attributable to the diminished release of latent heat, which is a consequence of water drainage facilitated by the geotextile.

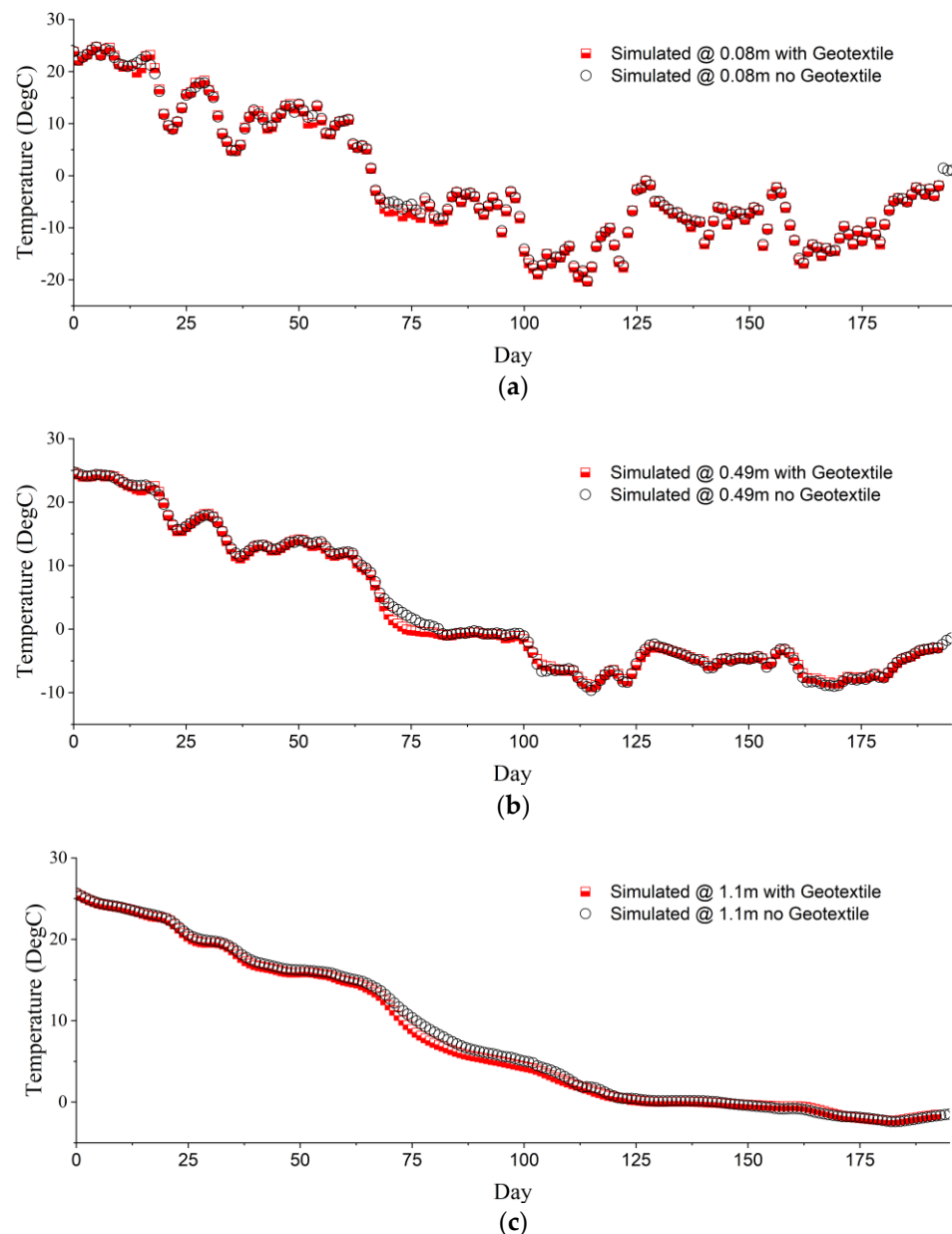


**Figure 13.** Simulated temperatures vs. time: (a) at 0.08 m in asphalt layer, (b) at 0.49 m in base layer, and (c) at 1.1 m in subgrade layer (along pavement axis of symmetry).

## 5. Conclusions

An advanced coupled model was developed to analyze pavements subjected to freezing climates. The model captures the coupled thermo-hydro processes within unsaturated frozen soils under pavement structure, and also accounts for environmental factors, including short-wave radiation, upward longwave radiation, air temperature, wind speed, relative humidity, ground heat flux, precipitation, ground water table (GWT), and evaporation. The accuracy of the model is validated by comparing the simulated temperature and moisture profiles with field data collected on the LTTP road section. The results confirmed its accuracy to provide comprehensive simulations of pavement structural responses to cold region climate considering unsaturated frozen soils.

The validated model was further applied to analyze the effects of wicking geotextile. The simulation results revealed that the wicking geotextile facilitated water absorption and drainage, and consequently changed water content (or suction) distributions in the

surrounding soils. In addition, the simulation results indicate that wicking geotextile delayed the onset of frost heave as well as reduced the magnitude of frost heave. While wicking geotextile reduces the liquid water contents and hence reduces the overall heat capacity, the simulation does not show apparent change of frost depth in the pavement. This might be due to the lower thermal conductivity induced by the replacement of water with air in the soil. Overall, the various effects of wicking geotextile on cold region pavements are simulated under various environmental dynamics using the comprehensive numerical model. This model provides a tool to temporally and spatially quantify the thermal-hydraulic processes induced by the wicking geotextile. The results of the simulations can serve as the bases for a more thorough and constructive guide for construction practices.

**Author Contributions:** Conceptualization, Y.J. and Z.A.; methodology, Y.J., Z.A., C.Z. and X.Y.; formal analysis, Y.J.; literature review, Z.A. and Y.J.; data acquisition, Y.J.; writing—original draft preparation, Y.J., Z.A. and X.Y.; writing—review and editing, Y.J., Z.A., C.Z. and X.Y. All authors have read and agreed to the published version of the manuscript.

**Funding:** This research was partially supported by the National Science Foundation (1638320) and National Cooperative Highway Research Program (01-59). This work is based in part of research funded by the National Academies of Science, Engineering, and Medicine Transportation Research Board’s (TRB) National Cooperative Highway Research Program (NCHRP) Project 01-59. The opinions, conclusions, and interpretations are those of the authors and not necessarily of NCHRP.

**Data Availability Statement:** The LTPP pavement data are available free of charge from the LTPP database. The simulation data are contained within the article and are free to use.

**Conflicts of Interest:** The authors declare no conflicts of interest.

## References

1. Mukhopadhyay, A.; Ye, D.; Zollinger, D. *Moisture-Related Cracking Effects on Hydrating Concrete Pavement*; Texas Transportation Institute, Texas A & M University System: College State, TX, USA, 2006; Volume 7.
2. Puppala, A.J.; Manosuthkij, T.; Nazarian, S.; Hoyos, L.R. Threshold Moisture Content and Matric Suction Potentials in Expansive Clays Prior to Initiation of Cracking in Pavements. *Can. Geotech. J.* **2011**, *48*, 519–531. [[CrossRef](#)]
3. Dong, S.; Jiang, Y.; Yu, X. A Novel Random Finite Element Model for Holistically Modeling of the Frost Effects on Soils and Cold Region Pavements. *J. Infrastruct. Preserv. Resil.* **2022**, *3*, 16. [[CrossRef](#)]
4. Liu, H.; Han, J.; Al-Naddaf, M.; Parsons, R.L.; Kakrasul, J.I. Field Monitoring of Wicking Geotextile to Reduce Soil Moisture under a Concrete Pavement Subjected to Precipitations and Temperature Variations. *Geotext. Geomembr.* **2022**, *50*, 1004–1019. [[CrossRef](#)]
5. Biswas, N.; Puppala, A.J.; Khan, M.A.; Congress, S.S.C.; Banerjee, A.; Chakraborty, S. Evaluating the Performance of Wicking Geotextile in Providing Drainage for Flexible Pavements Built over Expansive Soils. *Transp. Res. Rec.* **2021**, *2675*, 208–221. [[CrossRef](#)]
6. Guo, J.; Han, J.; Zhang, X.; Li, Z. Experimental Evaluation of Wicking Geotextile-Stabilized Aggregate Bases over Subgrade under Rainfall Simulation and Cyclic Loading. *Geotext. Geomembr.* **2021**, *49*, 1550–1564. [[CrossRef](#)]
7. Lin, C.; Zhang, X.; Galinmoghdam, J.; Guo, Y. Working Mechanism of a New Wicking Geotextile in Roadway Applications: A Numerical Study. *Geotext. Geomembr.* **2022**, *50*, 323–336. [[CrossRef](#)]
8. Zornberg, J.G.; Azevedo, M.; Sikkema, M.; Odgers, B. Geosynthetics with Enhanced Lateral Drainage Capabilities in Roadway Systems. *Transp. Geotech.* **2017**, *12*, 85–100. [[CrossRef](#)]
9. Lin, C.; Galinmoghdam, J.; Han, J.; Liu, J.; Zhang, X. Quantifying and Incorporating the Benefits of Wicking Geotextile into Pavement Design. *J. Transp. Eng. Part B Pavements* **2021**, *147*, 04021044. [[CrossRef](#)]
10. Wu, Y.; Ishikawa, T.; Maruyama, K.; Ueno, C.; Yasuoka, T.; Okuda, S. Modeling Wicking Fabric Inhibition Effect on Frost Heave. *Appl. Sci.* **2022**, *12*, 4357. [[CrossRef](#)]
11. Wu, Y. Effect Verification of Wicking Fabric on Inhibition to Frost Heave at Cold Region Pavement. Ph.D. Thesis, Hokkaido University Sapporo, Sapporo, Japan, 2022.
12. Guo, J.; Wang, F.; Zhang, X.; Han, J. Quantifying Water Removal Rate of a Wicking Geotextile under Controlled Temperature and Relative Humidity. *J. Mater. Civ. Eng.* **2017**, *29*, 04016181. [[CrossRef](#)]
13. Wang, F.; Han, J.; Zhang, X.; Guo, J. Laboratory Tests to Evaluate Effectiveness of Wicking Geotextile in Soil Moisture Reduction. *Geotext. Geomembr.* **2017**, *45*, 8–13. [[CrossRef](#)]
14. Lin, C.; Zhang, X. Laboratory Drainage Performance of a New Geotextile with Wicking Fabric. *J. Mater. Civ. Eng.* **2018**, *30*, 04018293. [[CrossRef](#)]
15. Zaman, M.W.; Han, J.; Zhang, X. Evaluating Wettability of Geotextiles with Contact Angles. *Geotext. Geomembr.* **2022**, *50*, 825–833. [[CrossRef](#)]

16. Zhang, X.; Galinmoghadam, J. *Performance of Wicking Geotextile on Mitigating Water Pumping Issue on I-44 Highway*; Department of Transportation, Construction and Materials Division: Kansas City, MI, USA, 2020.
17. Ud Din, I.M.; Mir, M.S.; Farooq, M.A. Effect of Freeze-Thaw Cycles on the Properties of Asphalt Pavements in Cold Regions: A Review. *Transp. Res. Procedia* **2020**, *48*, 3634–3641. [[CrossRef](#)]
18. Qiao, Y.; Dawson, A.R.; Parry, T.; Flintsch, G.; Wang, W. Flexible Pavements and Climate Change: A Comprehensive Review and Implication. *Sustainability* **2020**, *12*, 1057. [[CrossRef](#)]
19. Jiang, Y.; Yu, X. Holistic Multiphysics Simulation of the Climatic Responses of Cold Region Pavements. *J. Infrastruct. Preserv. Resil.* **2023**, *4*, 24. [[CrossRef](#)]
20. Krantz, W.B. A Generalized Secondary Frost. *SIAM J. Appl. Math.* **1994**, *54*, 1650–1675.
21. Zhan, Y.; Lu, Z.; Yao, H.; Xian, S. A Coupled Thermo-Hydromechanical Model of Soil Slope in Seasonally Frozen Regions under Freeze-Thaw Action. *Adv. Civ. Eng.* **2018**, *2018*, 7219826. [[CrossRef](#)]
22. Subramanian, S.S. Numerical Modelling and Geomechanical Analyses of Soil Slope Stability Evaluation in Seasonal Cold Regions. Ph.D. Thesis, Hokkaido University Sapporo, Sapporo, Japan, 2017; pp. 1–117.
23. Simonsen, E.; Isacsson, U. Thaw Weakening of Pavement Structures in Cold Regions. *Cold Reg. Sci. Technol.* **1999**, *29*, 135–151. [[CrossRef](#)]
24. Zhang, X.; Presler, W.; Li, L.; Jones, D.; Odgers, B. Use of Wicking Fabric to Help Prevent Frost Boils in Alaskan Pavements. *J. Mater. Civ. Eng.* **2014**, *26*, 728–740. [[CrossRef](#)]
25. Lin, C.; Presler, W.; Zhang, X.; Jones, D.; Odgers, B. Long-Term Performance of Wicking Fabric in Alaskan Pavements. *J. Perform. Constr. Facil.* **2017**, *31*, D4016005. [[CrossRef](#)]
26. Noborio, K.; McInnes, K.J.; Heilman, J.L. Two-Dimensional Model for Water, Heat, and Solute Transport in Furrow-Irrigated Soil: II. Field Evaluation. *Soil Sci. Soc. Am. J.* **1996**, *60*, 1010–1021. [[CrossRef](#)]
27. Konrad, J.M. Sixteenth Canadian Geotechnical Colloquium: Frost Heave in Soils: Concepts and Engineering. *Can. Geotech. J.* **1994**, *31*, 223–245. [[CrossRef](#)]
28. Hansson, K.; Šimůnek, J.; Mizoguchi, M.; Lundin, L.; Genuchten, M.T. Water Flow and Heat Transport in Frozen Soil: Numerical Solution and Freeze-Thaw Applications. *Vadose Zo. J.* **2004**, *3*, 693–704. [[CrossRef](#)]
29. Liu, X.; Rees, S.J.; Spitler, J.D. Modeling Snow Melting on Heated Pavement Surfaces. Part I: Model Development. *Appl. Therm. Eng.* **2007**, *27*, 1115–1124. [[CrossRef](#)]
30. Wang, C.; Ma, Z. Mathematical Model and Numerical Simulation of Hydrothermal Coupling for Unsaturated Soil Subgrade in the Seasonal Frozen Zone. *IOP Conf. Ser. Earth Environ. Sci.* **2021**, *719*, 032042. [[CrossRef](#)]
31. Li, N.; Chen, B.; Chen, F.; Xu, X. The Coupled Heat-Moisture-Mechanic Model of the Frozen Soil. *Cold Reg. Sci. Technol.* **2000**, *31*, 199–205. [[CrossRef](#)]
32. Coussy, O.; Monteiro, P. Unsaturated Poroelasticity for Crystallization in Pores. *Comput. Geotech.* **2007**, *34*, 279–290. [[CrossRef](#)]
33. Sweidan, A.H.; Niggemann, K.; Heider, Y.; Ziegler, M.; Markert, B. Experimental Study and Numerical Modeling of the Thermo-Hydro-Mechanical Processes in Soil Freezing with Different Frost Penetration Directions. *Acta Geotech.* **2022**, *17*, 231–255. [[CrossRef](#)]
34. Dong, S.; Jiang, Y.; Yu, X. Analyses of the Impacts of Climate Change and Forest Fire on Cold Region Slopes Stability by Random Finite Element Method. *Landslides* **2021**, *18*, 2531–2545. [[CrossRef](#)]
35. Anderson, D.M.; Tice, A.R.; McKim, H.L. Unfrozen Water and the Apparent Specific Heat Capacity of Frozen Soils. In *Second International Conference on Permafrost, Yakutsk, USSR*; North American Contribution; Wiley Online Library: Hoboken, NJ, USA, 1973; pp. 289–295.
36. Cass, A.; Campbell, G.S.; Jones, T.L. *Hydraulic and Thermal Properties of Soil Samples from the Buried Waste Test Facility*; United States Department of Energy, Pacific Northwest Lab: Washington, DC, USA, 1981; p. 23.
37. McInnes, K.J. Thermal Conductivities of Soils from Dryland Wheat Regions of Eastern Washington. MS Thesis, Washington State University, Washington, DC, USA, 1981.
38. van Genuchten, M.T. A Closed-Form Equation for Predicting the Hydraulic Conductivity of Unsaturated Soils. *Soil Sci. Soc. Am. J.* **1980**, *44*, 892–898. [[CrossRef](#)]
39. Koopmans, R.W.R.; Miller, R.D. Soil Freezing and Soil Water Characteristic Curves. *Soil Sci. Soc. Am. J.* **1966**, *30*, 680–685. [[CrossRef](#)]
40. Spaans, M. Monte Carlo Models of the Physical and Chemical Properties of Inhomogeneous Interstellar Clouds. *Astron. Astrophys.* **1996**, *307*, 271–287.
41. Deng, Q.; Liu, X.; Zeng, C.; He, X.; Chen, F.; Zhang, S. A Freezing-Thawing Damage Characterization Method for Highway Subgrade in Seasonally Frozen Regions Based on Thermal-Hydraulic-Mechanical Coupling Model. *Sensors* **2021**, *21*, 6251. [[CrossRef](#)]
42. Tang, T.; Shen, Y.; Liu, X.; Zhang, Z.; Xu, J.; Zhang, Z. The Effect of Horizontal Freezing on the Characteristics of Water Migration and Matric Suction in Unsaturated Silt. *Eng. Geol.* **2021**, *288*, 106166. [[CrossRef](#)]
43. Alavi, M.Z.; Pouranian, M.R.; Hajj, E.Y. Prediction of Asphalt Pavement Temperature Profile with Finite Control Volume Method. *Transp. Res. Rec.* **2014**, *2456*, 96–106. [[CrossRef](#)]
44. Huang, K.; Zollinger, D.G.; Shi, X.; Sun, P. A Developed Method of Analyzing Temperature and Moisture Profiles in Rigid Pavement Slabs. *Constr. Build. Mater.* **2017**, *151*, 782–788. [[CrossRef](#)]

45. Schlangen, E. *Online Help/Manual Module HEAT of FEMMASSE, 1990–2000*; Femmasse B.V.: Sittard, The Netherlands, 2000.
46. Morbidelli, R.; Corradini, C.; Saltalippi, C.; Flammioni, A.; Dari, J.; Govindaraju, R.S. Rainfall Infiltration Modeling: A Review. *Water* **2018**, *10*, 1873. [[CrossRef](#)]
47. Liu, Z.; Yu, X. Coupled Thermo-Hydro-Mechanical Model for Porous Materials under Frost Action: Theory and Implementation. *Acta Geotech.* **2011**, *6*, 51–65. [[CrossRef](#)]

**Disclaimer/Publisher’s Note:** The statements, opinions and data contained in all publications are solely those of the individual author(s) and contributor(s) and not of MDPI and/or the editor(s). MDPI and/or the editor(s) disclaim responsibility for any injury to people or property resulting from any ideas, methods, instructions or products referred to in the content.